Journal of *Marine Science and Engineering*

MDPI

Article

Design and Analysis of a Buoy-Based Cable Seafloor Observatory System Response under Extreme Weather Conditions

Wenjie Zhou [1,2], Yanjun Li [1,*], Yulu Zhang [1,2], Qingyan Jiang [2], Dong Chen [2], Yanzhen Gu [1,2,*] and Yuan Lin [2]

[1] Hainan Institute, Zhejiang University, Sanya 572025, China
[2] Ocean College, Zhejiang University, Zhoushan 316021, China
* Correspondence: yanjun.li@zju.edu.cn (Y.L.); guyanzhen@zju.edu.cn (Y.G.)

Abstract: In order to address the requirements of scientific multidisciplinary observation in diverse small-scale regions, we have introduced the Buoy-based Cable Seafloor Observatory System (BCSOS). This system offers a distinct advantage in contexts where the use of shorter cables is feasible, contrasting with the lengthy cables typically necessary for conventional observatories. The BCSOS consists of three primary components: the Real-Time Electric Communication (RTEC) Buoy, the Power Information Transmission System (PITS), and the Seafloor Observation Subsystem (SOS). The RTEC Buoy is equipped with instruments for measuring sea surface parameters and serves as a data and power hub. The PITS, comprising a robust EM cable, connects the buoy to the SOS, which houses instruments for seafloor observations. The system is designed for a maximum water depth of 100 m and has an expected lifespan of about 5 years. The BCSOS prototypes were deployed at the Huangqi Peninsula, Fujian Province, and successfully documented the process during Typhoon Doksuri (international code 2305) at the end of July 2023. The recorded data from the BCSOS revealed a significant increase in wave height and period as the storm approached the Huangqi Peninsula. Additionally, the RTEC buoy exhibited a notable response to the large waves. The data analysis revealed a distinct pattern between the buoy response and the direction of wave propagation across various sea conditions, that the buoy's angular movement in pitch and roll directions follows a regular elliptical distribution corresponding to different wave propagation directions. Upon thorough evaluation, future enhancements to the system are slated to concentrate on refining its design, with a particular emphasis on bolstering stability and enhancing corrosion resistance. These improvements are aimed at cementing the system's long-term viability and performance within the challenging marine environment.

Keywords: buoy response; typhoon doksuri; cable seafloor observatory; ocean multidisciplinary observation; wave propagation

Citation: Zhou, W.; Li, Y.; Zhang, Y.; Jiang, Q.; Chen, D.; Gu, Y.; Lin, Y. Design and Analysis of a Buoy-Based Cable Seafloor Observatory System Response under Extreme Weather Conditions. *J. Mar. Sci. Eng.* **2024**, *12*, 889. https://doi.org/10.3390/jmse12060889

Academic Editor: Angelo Rubino

Received: 1 March 2024
Revised: 10 May 2024
Accepted: 16 May 2024
Published: 27 May 2024

1. Introduction

Ocean observation is essential to human exploration, study, development, and utilization of the seas. The advancement of ocean observation technology is crucial for enhancing capabilities in monitoring the marine environment, predicting and alerting about ocean disasters, and increasing the capacity for marine resource development [1]. Currently, ocean observation consists of three parts: sea surface observation, profile observation, and seafloor observation [2]. Sea surface observation is mainly conducted through survey vessels, satellite remote sensing, and buoys [3–5]. Profile observation technologies, primarily using underwater gliders and profiling floats [6,7]. Seafloor observation is primarily conducted through Autonomous Underwater Vehicles (AUVs) and Cabled Seafloor Observatories [8,9].

Compared to survey vessels and underwater gliders, the observation technologies of AUVs, profiling floats, buoys, and cabled seafloor observatories enable in situ and long-term monitoring of marine environmental information. Satellite remote sensing provides

parameters only at the ocean surface and cannot observe changes within the ocean [10]. The cabled seafloor observation serves as an enduring system for monitoring the dynamics of the ocean process, facilitating high-bandwidth data transmission and supplying power to sensor networks, thereby ensuring a continuous flow of real-time information over extended periods. This sustained access to data is pivotal for the comprehensive understanding and observation of the subsurface marine environment, including the study of natural hazards such as earthquakes and tsunamis, which are of significant concern to the scientific community and society at large [11,12].

With the increasing demand for continuous fixed-point ocean observations, large-scale cabled seafloor observatory networks have been established in various countries [13], such as the Seafloor Observation Network for Earthquakes and Tsunamis (S-NET) [14] and Dense Oceanfloor Network system for Earthquakes and Tsunamis (DONET) [15] in Japan, the Ocean Networks Canada (ONC) [16], the Monterey Accelerated Research System (MARS) [17], the Ocean Observatories Initiative (OOI) [18] and the Integrated Ocean Observing System (IOOS) [19] in the United States, the European Multidisciplinary Seafloor and water-column Observatory (EMSO) in Europe [20], and the Integrated Marine Observing System (IMOS) in Australia [21] Cabled seafloor observatory networks are often characterized by substantial construction costs [22], which can be a limiting factor for their widespread implementation. Our team has designed a cost-effective cabled seafloor observatory system [23]. As illustrated in Figure 1, the cabled seafloor observatory system utilizes undersea cables to power and transmit data for seafloor observation equipment, enabling long-term monitoring and the acquisition of seafloor data.

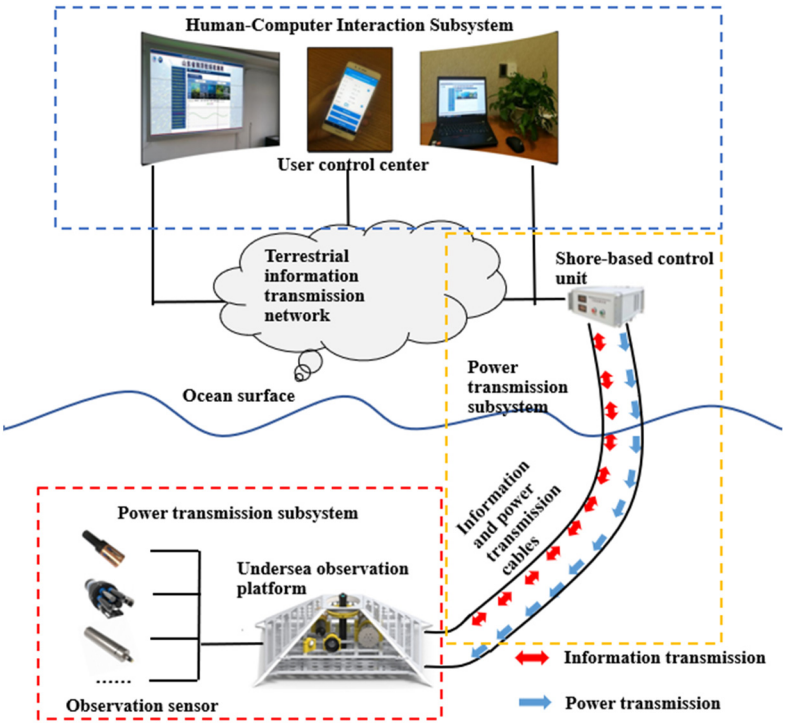

Figure 1. Cabled Seafloor Observatory System.

Given that the Seafloor Observatory Subsystem (SOS) is positioned at a considerable distance from the shoreline, it becomes imperative to make appropriate modifications to adapt to the extended reach. This entails not only lengthening the power transmission cable but also upgrading the voltage and augmenting the data transmission capabilities of the onshore control unit. Such enhancements are crucial for maintaining effective communication and operational efficiency over greater distances. This extension results in an escalation in manufacturing costs [24]. In light of these considerations, the Science Monitoring and Reliable Telecommunications (SMART) Subsea Cables initiative offers a promising solution

that could significantly impact deep ocean observing practices [25]. By integrating sensors into existing transoceanic telecommunications cables, this initiative has the potential to provide a more extensive and flexible framework for oceanographic research.

In this paper, we design a new type of cabled seafloor observatory named the Buoy-based Cable Seafloor Observatory System (BCSOS). The concept of Buoy based seafloor observatories was initially proposed by Mark Chaffey and Ed Mellinger of the MBARI, along with Walter Paul of the Woods Hole Oceanographic Institution [26]. Currently, various research institutions are putting forth different concepts for buoy-based seafloor observatories. The buoy-based seafloor observatories are mainly composed of buoys, submarine nodes, and mooring cables. These seafloor observatories are outfitted with an extensive suite of instruments, enabling comprehensive monitoring from the sea surface down to the ocean's most profound depths. The system's versatility stems from its modular architecture, which allows for customization of the structure, power supply, and communication networks to align seamlessly with the unique requirements of various research endeavors. They are equipped with different observation instruments, from the surface to the bottom of the sea. The system structure, power supply, and communication system can be redesigned according to the specific observation requirements, experiment duration, scientific payload, and research objectives.

The BCSOS relies on maritime buoys to position shore-based control units and is integrated with solar power systems to provide the necessary power to the seafloor observatory subsystem. The primary aim of this system is to establish a small-scale regional marine observatory designed for the seafloor and surface observation of the South China Sea, without the need for a shore power supply. This system can be employed for environmental monitoring in areas such as offshore marine ranches and coral reef regions. Due to its simplicity in deployment, the system can be relocated in case of emergencies with low operational costs.

The buoy is an essential component of the BCSOS, which provides space for batteries and communication instruments for power supply and data transmission [27]. The malfunction of the buoy will lead to a system-wide failure, so care must be taken with regard to the buoy response under extreme weather conditions. We collected and analyzed the data on buoy movement and waves including the data during the typhoon period to study the buoy response. This is an effective approach to understanding and evaluating buoy performance.

This paper is organized as follows: Section 2 provides an overview of the design of the BCSOS. Section 3 details the BCSOS deployment plan and field tests. Section 4 focuses on the in-depth analysis of the experimental data results from the sea trial, including data collected before, during, and after the typhoon, as well as the relationship between buoy responses and wave conditions. Finally, Section 5 concludes with a summary.

2. System Design

BCSOS technology is engineered to maximize the use of available proximity of the seafloor to the surface, offering a marked benefit in situations where the deployment of shorter cables is practical as opposed to the lengthy cables required by conventional observatories [12]. The conceptual design of the BCSOS consists of three primary components: the Real-Time Electric Communication (RTEC) Buoy, the Power Information Transmission System (PITS), and the Seafloor Observation Subsystem (SOS), as shown in Figure 2. The BCSOS has the capability to integrate various underwater observation devices. The RTEC buoy is equipped with instruments to measure pertinent sea surface parameters and also has real-time communication capability. The PITS can be equipped with profile observation equipment such as temperature chains. The SOS employs instruments specifically designed for seafloor observation. This collaborative configuration establishes a multidisciplinary real-time online observation system for continuous marine environment monitoring. This system is engineered to operate effectively in water depths of up to 100 m, with a design lifespan estimated at approximately five years.

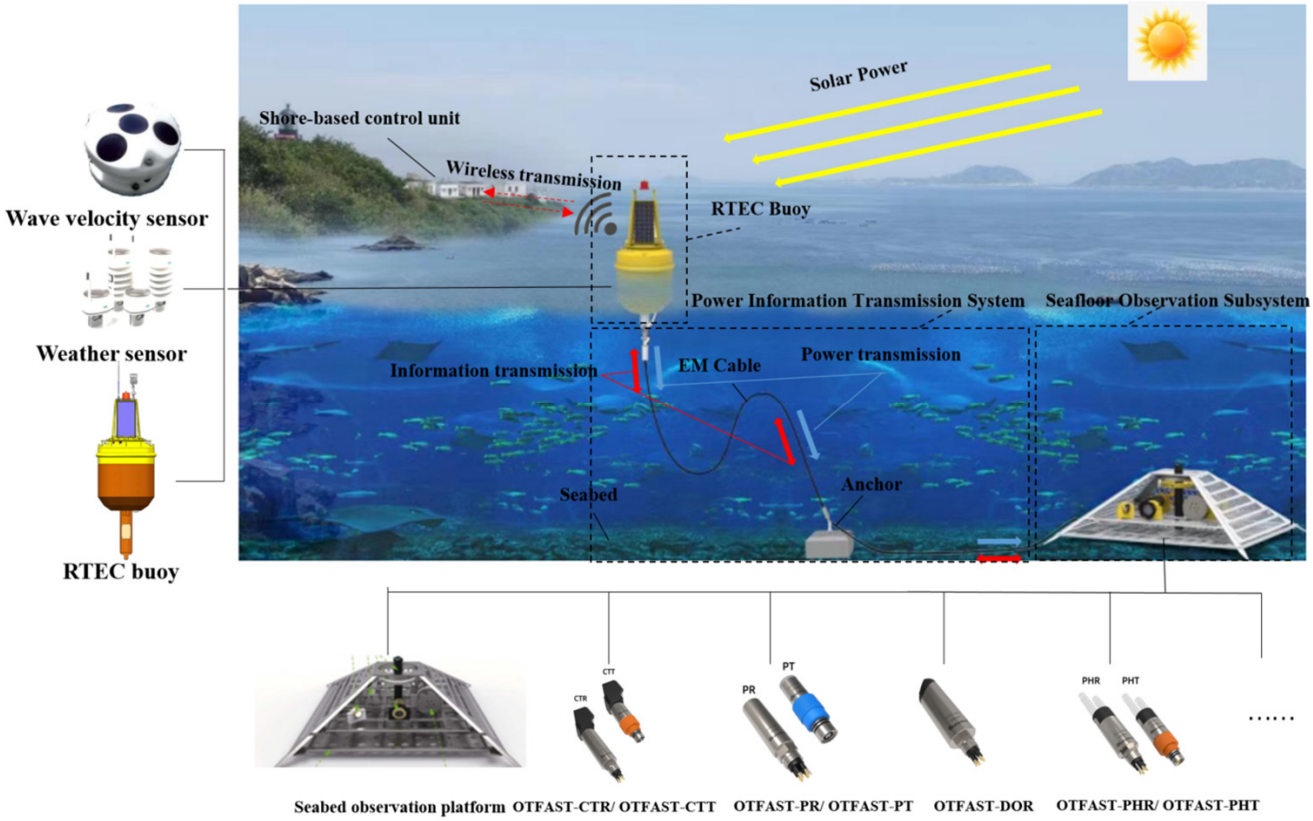

Figure 2. Concept design of Buoy-Based Cable Seafloor Observatory System (BCSOS).

2.1. Real-Time Electric Communication (RTEC) Buoy

The RTEC buoy is a core component of the BCSOS, responsible for transmitting data to the data center and supplying power to the SOS. Additionally, the buoy is equipped with instruments for measuring relevant parameters of the sea surface.

The RTEC buoy design encompasses a mechanical structure, power supply control equipment, sensors, and other electrical components. The mechanical structure serves as a protective barrier against harsh sea conditions, ensuring the buoy's stability.

The mounting plate situated on the buoy deck serves as a support for various components including the antenna, beacon light, meteorological instrument, lightning rod, and GPS, as shown in Figure 3. Additionally, the switch and data transmission port are also located on the buoy deck for accessibility. The buoy's hull is cylindrical in shape, providing space for the installation of control equipment and power supply components. Constructed from 316 L stainless steel, the buoy is resistant to corrosion, with its submerged area coated with an anti-corrosion coating. The buoy can also be made of aluminum or glass fiber-reinforced plastic to offer better corrosion resistance and durability over time [28]. As shown in Table 1, stainless steel exhibits greater strength compared to aluminum alloy. This enhanced strength is essential for preserving the structural integrity of the buoy, particularly in light of the frequent offshore fishing activities that are common in Chinese waters. Furthermore, an anode is installed to mitigate the corrosion process. Internally, the buoy features a sturdy structure comprising steel plates, angle steel, and a reinforced T-shaped steel framework, effectively preventing deformation when subjected to external forces.

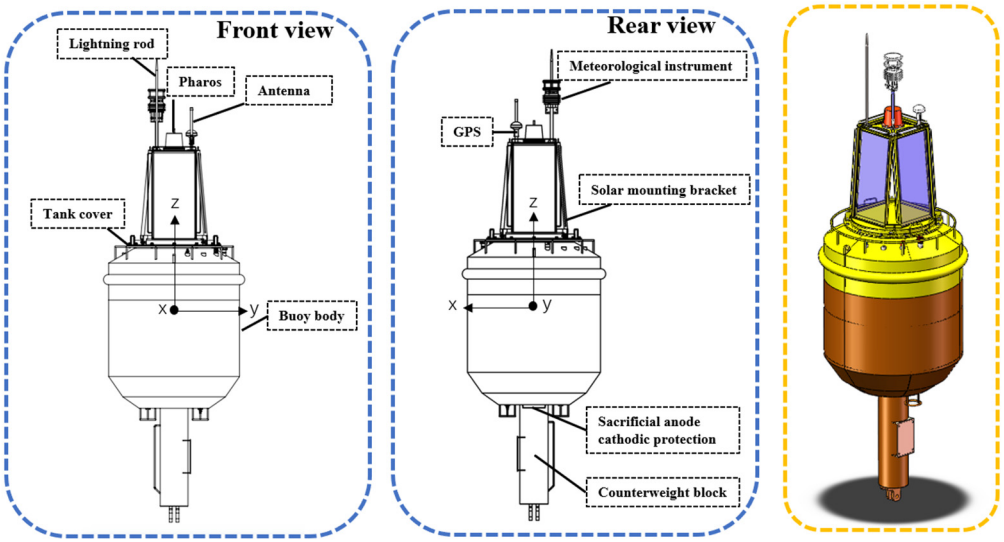

Figure 3. Real-Time Electric Communication (RTEC) Buoy structural details.

Table 1. Differences in properties between aluminum and stainless steel [29].

Material	Young's Modulus [MPa]	Melting Temperature [°K]	Electrical Resistivity [Ohm cm]	Density (Kg /cm^3)	Thermal Conductivity [W/m·°K]
Aluminum	72,000	823.15–923.15	193	0.0027	235
Stainless Steel	205,000	~1773.15	310	0.00785	79

The lower section of the buoy provides both ballast and space for housing the electro-mechanical (EM) cable. In addition, it contains a counterweight block, primarily utilized for the adjustment of the buoy's center of gravity (CG) to ensure that the buoy's CG remains situated below the center of buoyancy (CB) [30]. This configuration generates a righting moment essential for maintaining the buoy's stability. We have implemented an electrical slip ring (ESR) to facilitate the accommodation of cables from the RTC buoy and the SOS. The upper grey stator is connected to the buoy, and the lower rotor is connected to the cable. In the ESP, the current is transmitted through the contact between the carbon brush and the ring wire ring, forming a circuit in the sealed space between the stator and the rotor, so as to ensure the continuity of the current. The rotation of the rotor causes the wire to move in the magnetic field, and then transmits the electric energy and signal back to the stator side through electromagnetic induction. The ESR's main functions include preventing cable damage caused by torsion and facilitating power supply and communication transmission.

The RTC buoy's interior comprises the power supply system and the communication control system. The power supply system consists of photovoltaic solar panels, lithium battery packs, and the Maximum Power Point Tracking (MPPT) power control system responsible for supplying power to the instrument. The solar panel is encased in toughened glass with a light transmittance of not less than 90% and waterproof resin, with a conversion efficiency of 15%. The high-efficiency combination module comprises four 160 W/24 V solar panels and two 275 Ah/24 V rechargeable lithium batteries. Based on the estimated power consumption, two lithium batteries with a capacity of 6600 Wh can theoretically provide 6 months of endurance under the condition of solar panel failure. The lithium battery is equipped with a power intelligent management system. The communication control system comprises a control box responsible for overseeing the operational status of various instruments and equipment. It incorporates 4G/5G/microwave network transmission capabilities. The buoy with sensor interface can be equipped with instruments to facilitate continuous monitoring of sea surface environmental parameters such as wind speed, wind direction, air temperature, and humidity. Additionally, the system is equipped with a

substantial internal storage capacity of 128 gigabytes (GB). It captures and stores monitoring data and video footage, which are then relayed to the onshore control center through the buoy's control box. This data transmission is facilitated using the TCP/IP protocol and operates at a bandwidth of 6 megabits per second (Mbps).

Table 2 presents the design parameters of the RTC buoy. This design guarantees a reasonable metacentric height, which is initially determined as follows [31]:

$$Z_m = Z_b + r - Z_g \tag{1}$$

where, Z_m is the metacentric height. Z_b is the height of the center of buoyancy. r is the righting arm and Z_g represents the height of the center of gravity.

Table 2. The dimensions of the RTEC buoy.

Parameter	Unit	Value
Height of the Cover	m	0.07
Diameter of the Cover	m	0.69
Height of the Buoy Body	m	1.405
Height of the Mounting plate	m	0.79
Diameter of the Buoy Body	m	1.15
Height of the Counterweight	m	0.86
Diameter of the Counterweight	m	0.24
Height of the Buoy	m	3.265
Total Weight	kg	940

Taking the buoy draught line as the zero point, the vertical distance from the buoy's center to the horizontal plane is 0.637 m, and the distance from CG to CB is 0.136 m. The initial metacentric height of the buoy is established at 0.217 m. This configuration complies with the minimum requirement of 0.15 m for the initial metacentric height, as stipulated in the Classification Specification for Offshore Mobile Platform [32]. Subsequent refinements to the buoy design can lower its CG. For instance, extending the counterweight can increase the distance between the CG and the CB, thereby enhancing the buoy's stability and righting moment. This optimization improves the buoy's performance by mitigating the shaking motion it experiences, leading to more stable operations.

In the marine environment, buoys are primarily subjected to three main loads: wind, waves, and currents [33]. For the buoy design, we have considered the once-in-a-century typhoon scenario, characterized by a wind speed of 38 m/s, a flow velocity of 3 m/s, and a significant wave height of 10.5 m with a period of 11.53 s [34]. The subsequent section presents the theoretical calculation of the three loads.

In computing the wind load on the buoy, we opt to disregard the relatively minor force exerted in the vertical direction to make the calculation process more concise.

The equation describing the wind load exerted on the buoy structure is as follows [31]:

$$F_{\text{wind}} = P_w A_w \tag{2}$$

where, P_w represents the wind pressure exerted on the upper surface of the buoy, and A_w denotes the projection area perpendicular to the wind direction.

The wind pressure P_w is commonly derived from the reference wind pressure value P_0, with subsequent adjustments made to account for the fluctuation of wind pressure across different heights and the configuration of wind-exposed components. The reference wind pressure can be rewritten as:

$$P_0 = \frac{1}{2g}\gamma {v_{wind}}^2 \tag{3}$$

where, g represents the wind pressure exerted on the upper surface of the buoy. γ denotes the air density, $\gamma = 12.01$ N/m^3, v_{wind} is signifies the wind speed. Therefore, Equation (3) can be written as:

$$P_0 = 0.613{v_{wind}}^2 \tag{4}$$

The wind load calculation equation can be expressed as follows:

$$F_{\text{wind}} = \begin{bmatrix} F^x_{\text{wind}} \\ F^y_{\text{wind}} \end{bmatrix} = \begin{bmatrix} 0.613\beta C_H C_s {v_{wind}}^2 A_w \\ 0 \end{bmatrix} \tag{5}$$

where, F^x_{wind} is the component of wind load parallel to the horizontal plane. $\beta = 1.75$ is the power amplification factor. F^y_{wind} is the component of wind load perpendicular to the horizontal plane. C_H is the height coefficient of the change of the wind pressure along the height. Since the height of the buoy is below 15 m, $C_H = 1.0$. $C_s = 0.5$ is the wind component of the shape coefficient [31]. $A_w = 1.064$ m^2 is the projection area perpendicular to the wind direction, calculated using SolidWorks 2023, Student Edition. The wind speed is 38 m/s.

So,

$$F_{\text{wind}} = \begin{bmatrix} F^x_{\text{wind}} \\ F^y_{\text{wind}} \end{bmatrix} = \begin{bmatrix} 824.1N \\ 0 \end{bmatrix} \tag{6}$$

The calculation equation for the current load acting on the buoy structure is as follows [35]:

$$F_{\text{current}} = \begin{bmatrix} F^x_{\text{current}} \\ F^y_{\text{current}} \end{bmatrix} = \begin{bmatrix} \frac{1}{2}\rho A_d C_{dl} cos\alpha {v_{current}}^2 \\ 0 \end{bmatrix} \tag{7}$$

The current force is approximately calculated using the Morison equation. $\rho = 1025$ kg/m^3 is sea water density. $A_d = 1.238$ m^2 is the projection area perpendicular to the current direction. $C_{dl} = 0.4$ is water resistance coefficient. $\alpha = 0^\circ$ is the current angle as the maximum currents occur. $v_{current} = 3$ m/s is the current velocity.

So,

$$F_{\text{current}} = \begin{bmatrix} F^x_{\text{current}} \\ F^y_{\text{current}} \end{bmatrix} = \begin{bmatrix} 2284.1N \\ 0 \end{bmatrix} \tag{8}$$

The calculation equation for the wave load acting on the buoy structure is as follows [36]:

$$F_{\text{Wave}} = \begin{bmatrix} F^x_{\text{wave}} \\ F^y_{\text{wave}} \end{bmatrix} = \begin{bmatrix} \delta C_x H V_0 \frac{4\pi^2}{T^2} exp\left(-\frac{4\pi^2 D_{th}}{T^2 g}\right) \\ 0.5\delta C_y A^2 S_V \frac{4\pi^2}{T^2} exp\left(-\frac{8\pi^2 D_{th}}{T^2 g}\right) \end{bmatrix} \tag{9}$$

where $C_x = 2$ is the inertial coefficient relative to the horizontal plane, and $\delta = 104.49$ kg·s^2/m^4 is the water mass density. $H = 5$ is the maximum wave amplitude. $V_0 = 0.936$ m^2 is the buoy wet volume. $T = 11.53$ s is the wave period. $D_{th} = 1.314$ m is the draught depth. $C_y = 0.4$ is the inertial coefficient relative to the vertical plane. $S_V = 1.038$ m^2 is the area of the vertical plane.

So,

$$F_{\text{Wave}} = \begin{bmatrix} F^x_{\text{wave}} \\ F^y_{\text{wave}} \end{bmatrix} = \begin{bmatrix} 127.7N \\ 489.5N \end{bmatrix} \tag{10}$$

ANSYS is a widely recognized computational fluid dynamics (CFD) and finite element analysis (FEA) software used by engineers to simulate and analyze the structural integrity and fluid flow characteristics of complex systems [37]. We determined the external load under extreme weather conditions and utilized ANSYS simulation software (Ansys Student 2023 R1) to validate the buoy's ability to withstand harsh ocean environments as considered for static structural analysis. The buoy is designed using CAD software (Solidworks 2023, Student Edition), saved in IGES format, and subsequently imported into ANSYS for analysis, with its principal dimensions displayed in Figure 4. The mesh was divided into tetrahedral elements, with an overall unit size of 0.03 m and a total of 180,358 elements. The

simulation employs the Solid187 element type, a tetrahedral finite element within ANSYS that consists of 10 nodes.

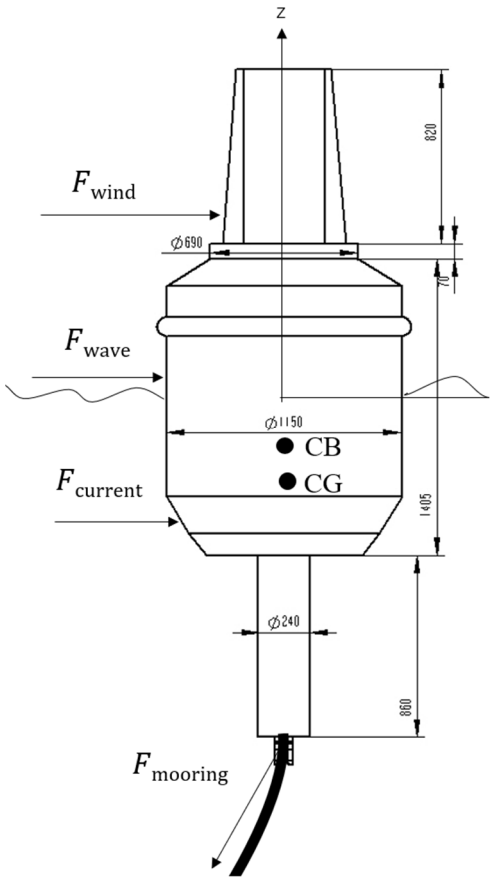

Figure 4. Simplified size of RTEC buoy.

A remote displacement boundary condition was applied to the surface of the ring at the buoy's waterline. The lower part of the buoy's waterline was subjected to waves and currents, while the upper part was affected by wind loads. The structural weight and the internal equipment were evenly distributed on the bottom surface of the structure, with the surrounding environment experiencing hydrostatic pressure.

The results indicate that the maximum equivalent pressure on the buoy occurs at the junction of the buoy body and the counterweight, with a maximum stress of 54.937 MPa. Given that the outer surface of the buoy is made of 316 L stainless steel, and its yield strength is 172 MPa. The safety factor of the buoy is 1.5, and the allowable stress of the material is 113.3 MPa. Therefore, the buoy design is safe based on the perspective of allowable stress.

The maximum deformation of the buoy is observed at the bottom of the counterweight, with a maximum deformation of 1.889 mm, which is negligible. To verify grid independence, we further refined the mesh, resulting in a total of 352,451 elements. The maximum equivalent pressure is 54.658 MPa, which is observed at the junction of the buoy's counterweight. The error of the results is considered reasonable, and the credibility of the simulation results is not influenced by grid density.

In conclusion, the static structural simulation results affirm that the designed buoy structure meets the strength design requirements of marine structures.

2.2. Power Information Transmission System (PITS)

The PITS consists of the EM cable and the heavy structure of the buoy. The EM cable serves as the connection link between the surface buoy and the SOS.

The EM cable comprises two layers of polyethylene (PE) sheathing, each with a thickness of 4 mm. The cable utilizes a dual-core copper conductor for signal transmission, featuring a cross-sectional area of 2.5 mm², and supports an information transmission rate of 6.3 Mbps. Additionally, two layers of galvanized steel wire, measuring 2.0 mm and 2.7 mm, respectively, are sandwiched in the middle to enhance cable protection. This construction results in an overall diameter of 34 mm. The properties of the EM cable are shown in Table 3.

Table 3. Properties of the EM cable.

Cable Properties	Unit	Nominal Value
Diameter	mm	34 ± 0.5
Air weight	kg/m	1.5 ± 0.1
Minimum breaking strength	kN	240
Maximum working load	kN	100
Safe working load	kN	50

To ensure that the EM cable has sufficient strength for secure mooring to a buoy, a series of tensile tests are performed. Initially, the cable is subjected to three cycles of testing at its rated safe working load of 5 tons. This step is critical for evaluating the cable's stability and axial stiffness under safe load conditions. Subsequently, the cable's breaking load is determined through further testing. The test outcomes validate that the EM cable is capable of withstanding operational loads, exhibiting an axial stiffness of 6476 kN during the 5 ton load test and a minimum breaking strength of 247.2 kN. These results affirm the cable's reliability and safety for use in mooring applications.

To mitigate the risk of fatigue fracture or excessive tension failure at the cable-buoy connection, as illustrated in Figure 5, a load-bearing structure is incorporated into the EM cable design. After assembly, it can be filled with epoxy resin and integrated with the transmission cable to increase the connection performance. This structure is engineered to withstand forces of up to 200 kN of force, thereby preventing potential failure of cable-buoy connections due to high tension.

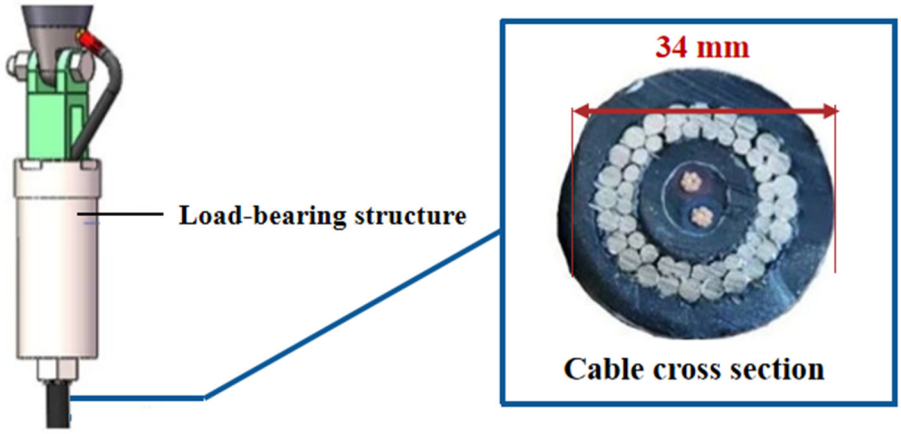

Figure 5. The structure of PITS.

Moreover, there exists a possibility that the cable could exert a dragging force on the SOS, potentially leading to its unintended lifting. To counteract this effect, the use of an anchor is crucial. It serves to prevent the inadvertent lifting of the SOS and to ensure stable and reliable anchoring to the seafloor.

To ensure the EM cable's safety under extreme conditions, potential theory is frequently employed as a standard numerical tool for analyzing the hydrodynamic behavior of structures in wave environments. AQWA software (Aqwa 2023 R1) employs a hybrid method to model the large volume components of a structure by diffracting panels and

the small cross-sectional components by Morison elements [38]. Specifically, AQWA is deployed to simulate and analyze the cable tension within the BCSOS under extreme sea conditions. The buoy's hydrostatic parameters are presented in Table 4. The X, Y, and Z directions of the sea were represented using this model box of 200 m × 200 m × 100 m that replicates the fully developed sea condition.

Table 4. The buoy's hydrostatic parameters.

Parameters	Value
Centre of Gravity (x, y, z)	(0, 0, −0.637 m)
Mass (kg)	940
Area (m^2)	438.49
Volume (m)	344.98
Moment of Inertia, I_{zz} (Kg·m^2)	107.44
Moment of Inertia, I_{xx} (Kg·m^2)	600.36
Moment of Inertia, I_{xx} (Kg·m^2)	602.58

In the establishment of simulated environmental conditions, we have incorporated the JONSWAP spectrum, a model that characterizes the statistical distribution of ocean surface wave height and period [39], and the Norwegian Petroleum Directorate (NPD) wind spectrum to reproduce the effect of wave and wind. In view of the extremely low water velocity near the seabed, the impact on the system is negligible. We assume that the water velocity decreases linearly from the sea surface to the seabed to zero, the directions of wind, ocean currents, and waves are in the same direction. For the simulations, we have taken into account a once-in-a-century typhoon scenario, with the specific parameters outlined in Table 5. In the JONSWAP spectrum, the parameter GAMMA represents the non-dimensional peak frequency and is instrumental in modeling the distribution of wave energy across the spectrum.

Table 5. The parameters settings of environmental conditions.

Parameter	Value
Current Speed (Sea Surface)	3 m/s
Wind Speed (NDP)	32 m/s
Significant Wave Height (JONSWAP)	11.53 m
Wave Peak Period	13 s
Gamma (JONSWAP)	3.3

The cable parameters for the simulation are configured in accordance with the experimental data presented in Table 6. The simulation results indicate that the maximum force experienced by the cable is 41.91 kN, which is well below its maximum working load capacity. This finding affirms the rationality and safety of the EM cable design.

Table 6. The cable parameters.

Parameters	Value
Equivalent Diameter (m)	0.034
Transverse Drag Coefficient	1.20
Longitudinal Coefficient	0.025
Mass per unit length (kN/m)	1.5
Stiffness, EA (kN)	6476.19
Cable length (m)	160
Maximum Expected Tension (kN)	272.2

2.3. Seafloor Observation Subsystem (SOS)

The SOS is designed to be fixed on the seafloor, accommodating sensors, cameras, and instruments to facilitate continuous data monitoring and collection, as depicted in Figure 6. The SOS frame is constructed with a corrosion-resistant 316 L stainless steel frame, which ensures long-term durability. The sensors are securely installed using nylon clips and are equipped with a sacrificial anode to prevent electrochemical corrosion between different metals.

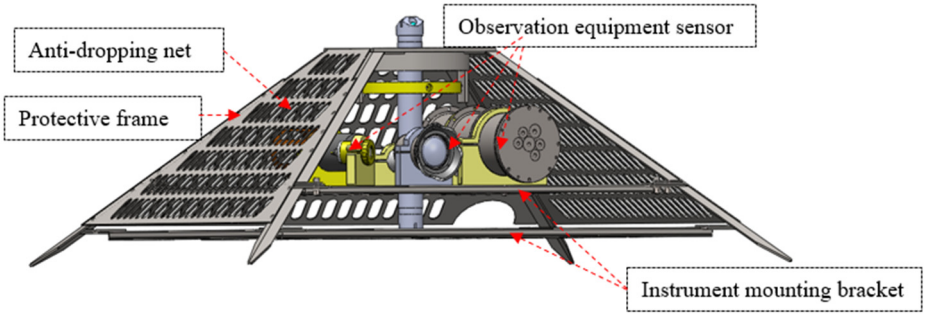

Figure 6. The structure of SOS.

The SOS frame is engineered with pointed support feet that are intended to penetrate the seabed, thereby providing a stable foundation to enhance the system's stability. The dimensions of the SOS are approximately 1.7 m × 1.7 m × 0.6 m, with an overall weight of about 170 kg, inclusive of both the frame and instruments. The outer cover is designed to be anti-trawling, enhancing resistance to bottom currents and reducing the risk of entanglement with fishing nets.

The scientific payload of the SOS encompasses a Multiparameter water quality meter, an Acoustic Doppler Current Profiler (ADCP), an Underwater camera, an Underwater LED lamp, and UV lamps. The OTSwitch-DR Multiparameter Water Quality Meter is designed to be fitted with various sensors to measure water quality parameters as per detection requirements, with a maximum sampling frequency of 25 Hz. The Aquadopp Profiler, operating at 1 MHz, is a versatile ADCP capable of measuring the velocity and direction of ocean currents, with a maximum profiling range of up to 25 m. The OTSphyrna-500 Underwater Camera is utilized for visual observation and documentation of seafloor and water column conditions, offering a high-definition resolution of 1920 × 1080. The OTSUN Underwater LED Lamp is specifically engineered to provide illumination for the OTSphyrna-500 in low-light conditions. To mitigate biological fouling on the underwater camera, two OTUVpro UV Lamps are employed. The sealed control cabin, constructed from titanium, is engineered to resist pressures up to 6.25 MPa and is equipped with an internal heatsink to effectively manage the thermal requirements of the power supply system. A CAN bus distributed modular management system has been integrated, ensuring the complete isolation of power supply and communication pathways between individual sensors. This design enables independent power management and data acquisition control for the underwater integrated instruments, enhancing the system's efficiency and reliability.

2.4. BCSOS Power Consumption

The total daily power consumption of the BCSOS is approximately 136 watt-hours (Wh), and the energy is allocated between two primary subsystems: the RTEC buoy and the SOS.

The RTEC buoy subsystem is integrated with components that cumulatively account for a daily power consumption of 92 Wh. Significant power consumers in the RTEC buoy include the control board, power control panel, five-port switch, bridge, voltmeter/ammeter, 4G router, and GPS module. For the SOS, the power consumption varies according to the devices carried. Essential components in this regard include the underwater ARM board, power control panel, bridge, and various seabed equipment like the multiparameter water

quality meter, ADCP, underwater camera, LED, and UV lamps. For a detailed breakdown of the power consumption of each component, please refer to Table 7.

Table 7. BCSOS power consumption statistics.

Type	Hardware/Instrument	Voltage/Average Current	Working Frequency	Power Consumption
RTEC Buoy	ARM board	Voltage 12 V, Average current 0.15 A	24 h	43.2 Wh
	Power control panel	Voltage 24 V Average current 0.023 A	24 h	13.25 Wh
	Switch	Voltage 12 V, Average current 0.167 A	Works for 5 min every 1 h, 2 h per day	4 Wh
	Bridge	Voltage 12 V, Average current 0.35 A	Works for 5 min every 1 h, 2 h per day	8.4 Wh
	hybrid transmission module	Voltage 24 V, Average current < 0.001 A	-	-
	Voltmeter/Ammeter	Voltage 12 V, Average current 0.035 A	24 h	20.16 Wh
	4G router	Voltage 12 V, Average current 0.1 A	Works for 5 min every 1 h, 2 h per day	2.4 Wh
	GPS module	Voltage 12 V, Average current 0.035 A	Works for 5 min every 1 h, 2 h per day	0.6 Wh
Seafloor Observation Subsystem (SOS)	Underwater ARM board	Voltage 5 V, Average current 0.28 A	Works for 5 min every 1 h, 2 h per day	2.8 Wh
	Power control panel	Voltage 24 V, Average current 0.01 A	Works for 5 min every 1 h, 2 h per day	0.48 Wh
	Bridge	Voltage 12, Average current 0.35 A	Works for 5 min every 1 h, 2 h per day	8.4 Wh
	hybrid transmission module	Voltage 24 V, Average current < 0.001 A	-	-
	Multiparameter water quality meter	Voltage 12 V, Average current 0.01 A, Peak current 0.9 A	Works for 5 min every 1 h, 2 h per day	12 Wh
	Acoustic Doppler Current Profiler	Voltage 15 V, Average current 0.25 A	Works for 5 min every 1 h, 2 h per day	7.5 Wh
	Underwater camera	Voltage 12 V, Average current 0.5 A	Works for 5 min every 3 h	4 Wh
	Underwater LED lamp	Voltage 24 V, Average current 0.538 A	Works for 5 min every 3 h	8.61 Wh
	UV lamp	Voltage 12 V, Average current 0.072 A	Works for 5 min every 3 h	0.576 Wh

Upon deployment, the average daily solar energy yield from four 160 W/24 V solar panels in the specified deployment zone (26°17′ N, 119°50′ E) fluctuates between 250 to 350 Wh. This output is adequate to energize the entire system, allowing for self-sustained operation and minimizing the need for frequent recharging cycles. Regarding the system's suitability for different latitudes and environmental conditions, the current design with a limited surface area of solar panels may not be sufficient for regions with low solar energy availability, such as the Arctic with its very little and seasonal solar energy as the weather in September turns cold, cloudy and rainy, the potential of solar photovoltaic power generation decreases, especially in December and January [40], and the energy consumption of lithium batteries will also increase in cold regions [41]. It is possible to further improve the self-sufficiency of the power generation system by using wind and wave energy of other power generation devices.

3. Experimental Study

In this section, we elaborate on the deployment of the BCSOS near the Huangqi Peninsula in Fujian Province, China. The BCSOS was deployed in the East China Sea at coordinates 26°17′ N, 119°50′ E, on 9 June 2023.

The deployment of the BCSOS necessitates the attachment of a 1 ton cement block as an anchor to the cable to prevent the SOS from being dragged upwards by the RTEC buoy. Additionally, the counterweight fulfills another role by incorporating a saddle-shaped support to minimize friction with the seabed and provide guidance for the upward movement of the cable. Floats are essential components of the "S" mooring cable to keep it buoyant in the water and prevent abrasion on the seabed. The "S" refers to the shape of the mooring cable, which is kept buoyant in the water by floats [42]. The deployment schematic is illustrated in Figure 7.

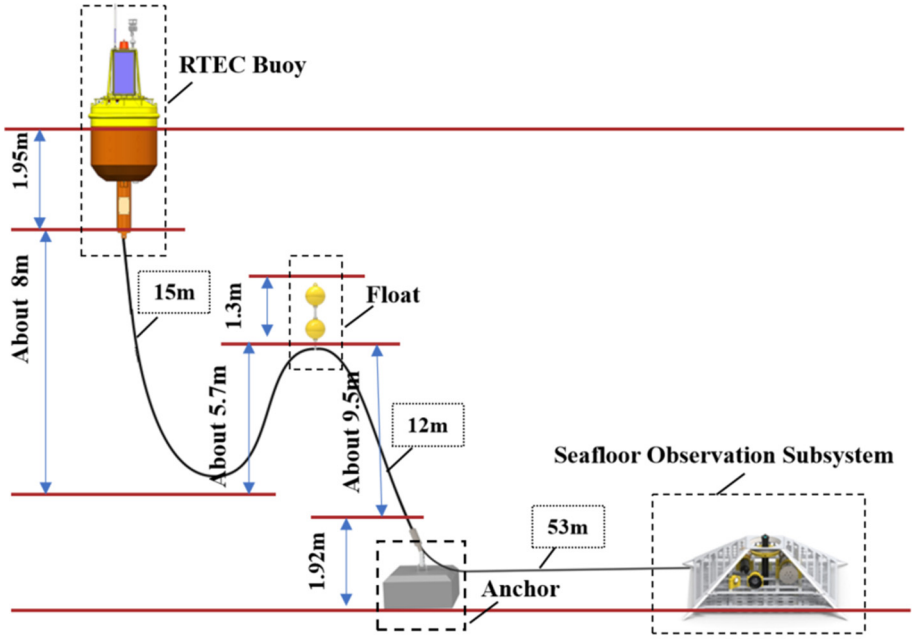

Figure 7. The BCSOS deployment schematic.

The EM cable establishes the connection between the buoy and the observation system, with a total length of 80 m. Concurrently, the buoy is equipped with the 6-axis GPS-IMU, which features a built-in gyroscope, accelerometer, and GPS, facilitating the measurement of the buoy's attitude.

On 9 June 2023, amidst the Pacific typhoon season, the BCSOS was successfully deployed. The system ensemble included an RTEC buoy, floats, a cement block for anchoring, an EM cable for transmission, and a SOS for continuous marine environment monitoring.

During deployment, we first completed the installation and debugging of the BCSOS at the wharf. Considering the boat's restricted lifting capacity, we positioned the cement block and the RTEC buoy on the boat's sliding deck. Initially, we employed a derrick to deploy the SOS to the designated seabed location, under the guidance of a diver. During this phase, it was crucial to ensure that the length of the EM cable extending from the SOS to the cement block was sufficient for deployment, as the cement block remained secured to the boat. Subsequently, we released the cement block. Once the cement block descended to its predetermined position, we manually lowered the float and cable. The final procedure was to release the RTEC buoy, thereby completing the deployment of the BCSOS. The deployment process is shown in Figure 8.

Step1: Prepare BCSOS

Step2: Deploy the seafloor observation subsystem down towards the destination seabed

Step3: Deploy cement hwavy block, lay cable and floats down

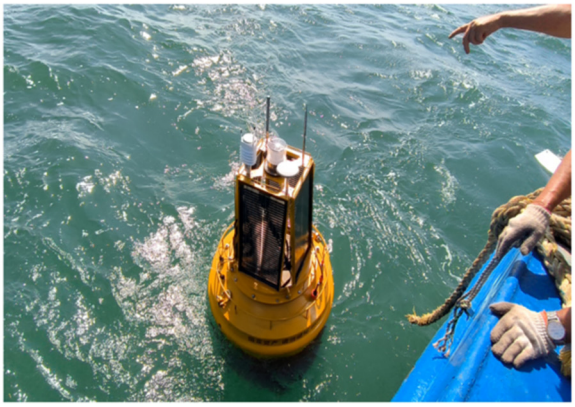

Step4: Deploy the Real-Time Electric Communication (RTEC) buoy

Figure 8. The process of deploying the BCSOS.

The deployment of BCSOS was successful, as on-site observations confirmed the buoy's smooth operation. No malfunctions were detected, indicating that the communication link between the RTEC buoy and SOS is normal. The transmitted conductivity, temperature, and depth data indicated that the SOS deployed location is approximately 16.9 m deep. In the evening, the connection of the camera, underwater LED lights, and the camera itself were successfully verified, confirming the normal operation of the BCSOS.

After deployment, the BCSOS continues to operate on-site. On 28 July 2023, Typhoon Doksuri (International Number 2305) made landfall on the coastal areas of Jinjiang, Fujian, with winds reaching 50 m/s (180 km/h) [43]. In close proximity to the BCSOS location, the BCSOS successfully monitored the significant changes in various environmental parameters induced by the typhoon. As depicted in Figure 9, the BCSOS operated normally despite the influence of Typhoon Doksuri.

The scheduled maintenance interval for the buoy base is set to six months, with the most recent maintenance conducted on 5 April 2024. The primary objectives of this routine maintenance include a thorough inspection of various system components, such as: evaluating the integrity and performance of the solar panels to confirm they remain undamaged and efficient, examining the underwater connecting cable for any indications of wear or damage, assessing the sacrificial anode for signs of corrosion to determine if replacement is necessary, and servicing the underwater instruments to ensure their ongoing accuracy and operational functionality. These maintenance activities are crucial for the reliable performance and extended lifespan of the BCSOS. Proactive inspections and servicing enable prompt identification and resolution of potential issues, thereby reducing the likelihood of system downtime and ensuring uninterrupted operation. After 10 months

of deployment, all system components have demonstrated stable operation. However, biological fouling was observed on both the buoy and the SOS, as seen in Figure 10. Notably, the installation of UV lights at the camera significantly mitigated biological attachment compared to other components. According to the previous simulation results of ANSYS, the stress at the joint may lead to the main structural fatigue over time. Therefore, during this maintenance period, we focused on this area and found that a large number of biological growth areas appeared at the junction between the ESR structure and the buoy body. The presence of substantial marine growth in this region could potentially compromise the ESR's performance and the structural fatigue of the accelerating buoy. This observation highlights the significance of strategic maintenance initiatives, including the application of anti-fouling treatments and regular cleaning of susceptible areas. Such measures are essential for preserving the long-term dependability and efficiency of the BCSOS within the demanding marine environment.

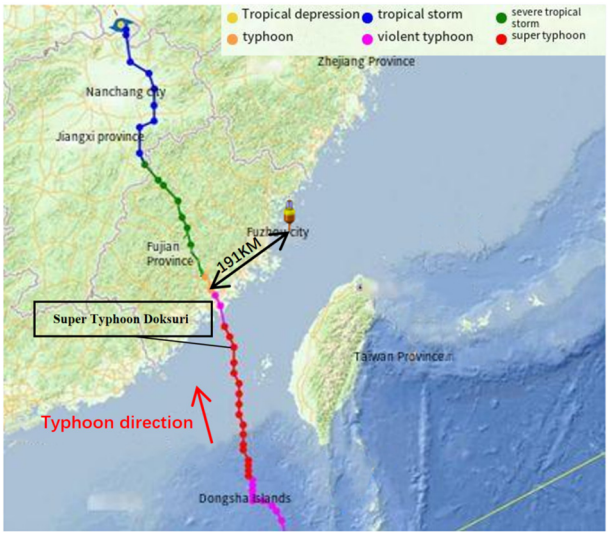

Figure 9. The path of Typhoon Doksuri.

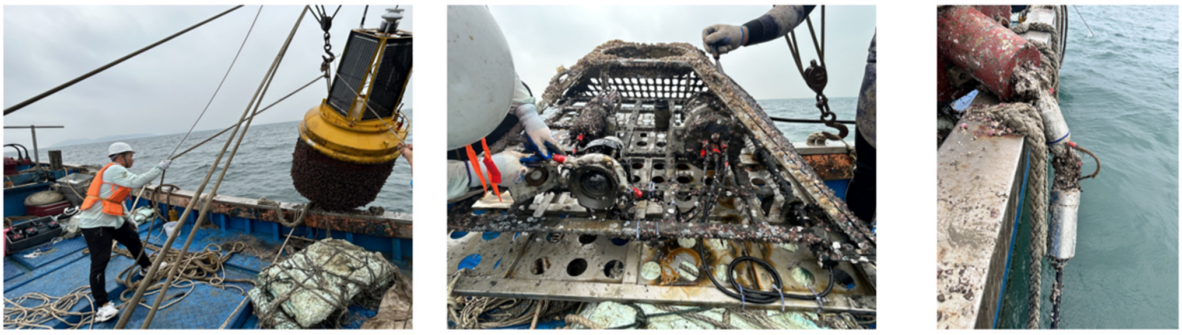

Figure 10. (**a**) Recovered RTEC buoy; (**b**) Recovered SOS; (**c**) The joint between the ESR structure and the buoy body.

In summary, the BCSOS has undergone rigorous testing under challenging sea conditions. The total expenditure for deploying the BCSOS is estimated to be less than USD 2500. This indicates a considerable decrease in the costs associated with deployment when compared to traditional observatories, thereby providing a more financially feasible approach to the implementation of seafloor observation systems. The BCSOS has maintained stable operation to the present day, further substantiating the soundness of its design principles. Notably, the system successfully captured the buoy's response to wave-induced motion during Typhoon Doksuri, and the findings will be elaborated in the results section.

4. Analysis of the BCSOS Behavior at the Typhoon Passage

In this section, we present the experimental data of the BCSOS before, during, and after Typhoon Doksuri. The experiment data illustrate the response of the RTEC buoy response to wave excitation. Additionally, by setting the incident direction of the wave, we study the relationship between the incident angle of the wave height and the response of the buoy.

4.1. Wave Conditions

The RTEC Buoy recorded the wave conditions over an 8-day span from 23 July 2023 to 30 July 2023, around the time of Typhoon Doksuri's passage. The recorded wave height represents the significant wave height, and the period denotes the period of the significant wave. Throughout this duration, the sea conditions observed can be categorized into four distinct sections: the normal sea period from July 23 to July 24, the pre-typhoon period from July 25 to July 26, the during-typhoon period from July 27 to July 28, and the post-typhoon period from July 29 to July 30.

Based on the data presented in Figure 11, a noticeable increase in wave height is observed during the pre-typhoon period (25–26 July) compared to the normal sea period (23–24 July). This increase is attributed to the influence of typhoon Doksuri approaching the BCSOS deployment location. The average wave height increased from 0.28 m to 0.70 m, and the average period increased from 3.22 s to 3.68 s. During the typhoon period from 27 to 28 July, the average wave height further increased to 1.33 m, accompanied by an increase in the period to 5.14 s. Notably, the maximum wave height peaked at 2.41 m during the passage of Typhoon Duksuri, with a period of 6.46 s. The influence of the typhoon resulted in significant increases in both the wave height and period. Generally, larger wave heights are accompanied by longer wave periods, indicating more regular and larger waves. Subsequently, during the post-typhoon period, the average significant wave height decreased to 0.64 m, with a period of 5.28 s. The decrease in wave height compared to the previous period is notable and suggests a shift in sea conditions following the passage of Typhoon Duksuri.

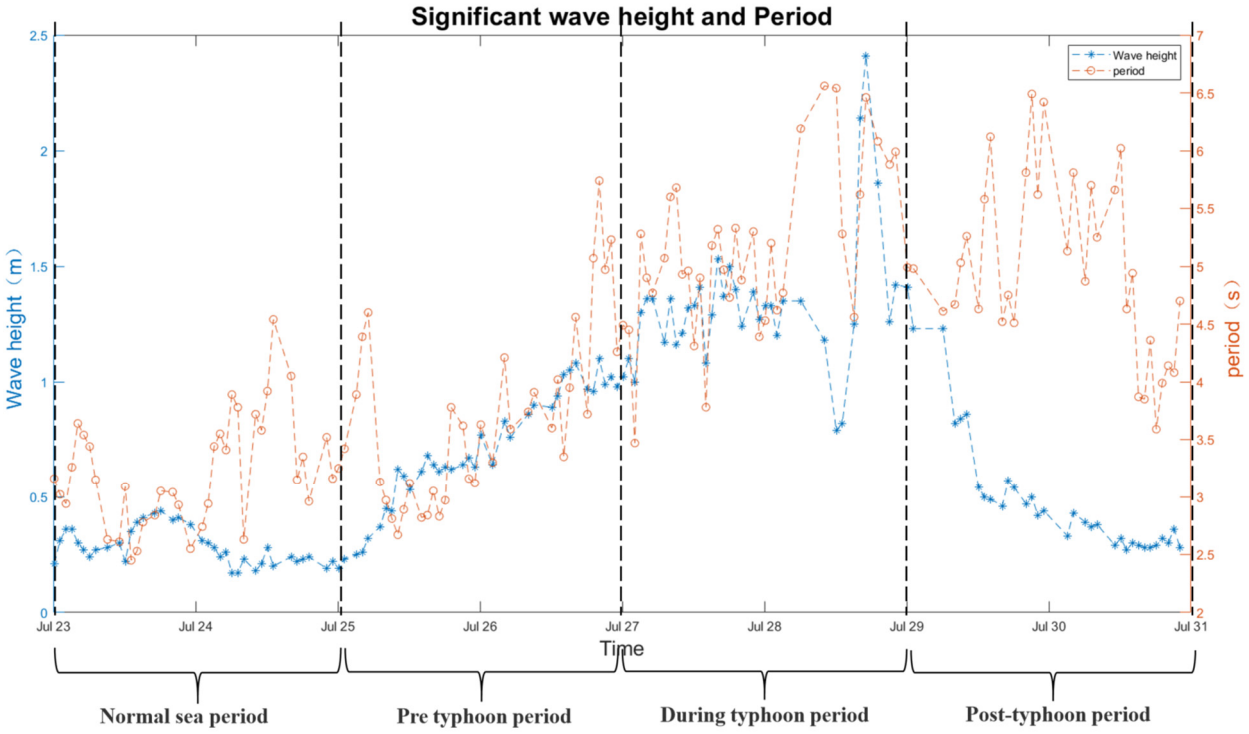

Figure 11. The significant wave height and wave period recorded from 24 to 30 July.

4.2. Response of Buoy

The response of the buoy is depicted in Figure 12, revealing a trend similar to that of the wave height across the four periods. During the pre-typhoon period, the buoy exhibited an upward trend in response, with the peak values of roll and pitch remaining below 30°. As the typhoon approached, the buoy response intensified, with most peaks reaching values within 40°. Following the passage of Typhoon Duksuri, the buoy response quickly returned to normal sea conditions.

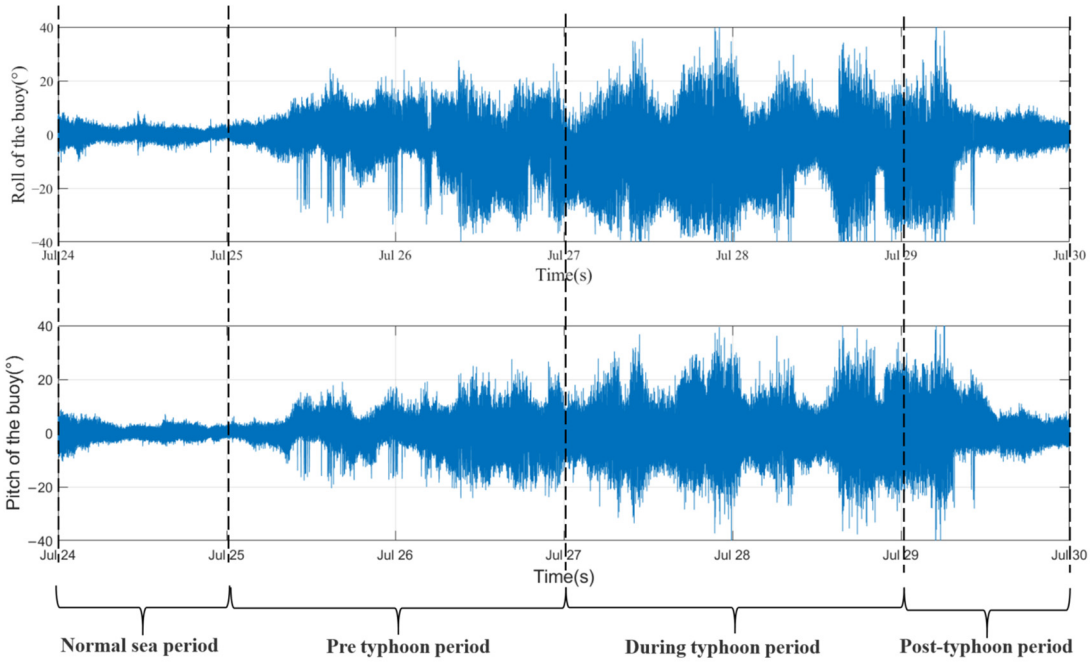

Figure 12. Buoy response recorded from July 24 to 30.

The mean absolute value (MAV) of the buoy's response across four distinct periods is concisely summarized in Table 8. In this context, the MAV of the buoy's response is utilized to denote the amplitude of the buoy's response. It is evident that during the typhoon period, the MAV of roll is 9.20 times higher than during the normal period, while the MAV of pitch is 4.36 times higher. Such a substantial increase in buoy response during the typhoon period raises concerns about the potential for repeated bending of the underlying cable connections, which could lead to fatigue damage. This underscores the importance of addressing this issue to prevent any structural complications.

Table 8. MAV of buoy response in the four periods.

Period	Roll	Pitch
Normal sea	1.19°	1.09°
Pre-typhoon	5.55°	3.51°
During-typhoon	9.98°	5.59°
After-typhoon	5.19°	4.32°

4.3. Impact of Waves on the Distribution of Buoy Response under the Influence of Different Waves

In this section, we examine the relationship between the distribution of roll and pitch values and the incident angles of waves. To explore this relationship, we categorize the incident angles of waves recorded by the buoy during the BCSOS operation from July to August. Given that the measured wave height is averaged over 10 min intervals, the buoy response distribution is also segmented into 10 min intervals, resulting in 600 data points.

When plotting the roll of the buoy on the abscissa and the pitch on the ordinate, Figure 13 illustrates that the distribution area of roll and pitch may exhibit an elliptical shape when the incident wave direction is 0°, 45°, 90°, and 135°. In Figure 13, "Wave" denotes the wave height, while "T" represents the wave period. It is worth noting that the buoy's elliptical response rotates in synchrony with shifts in wave direction.

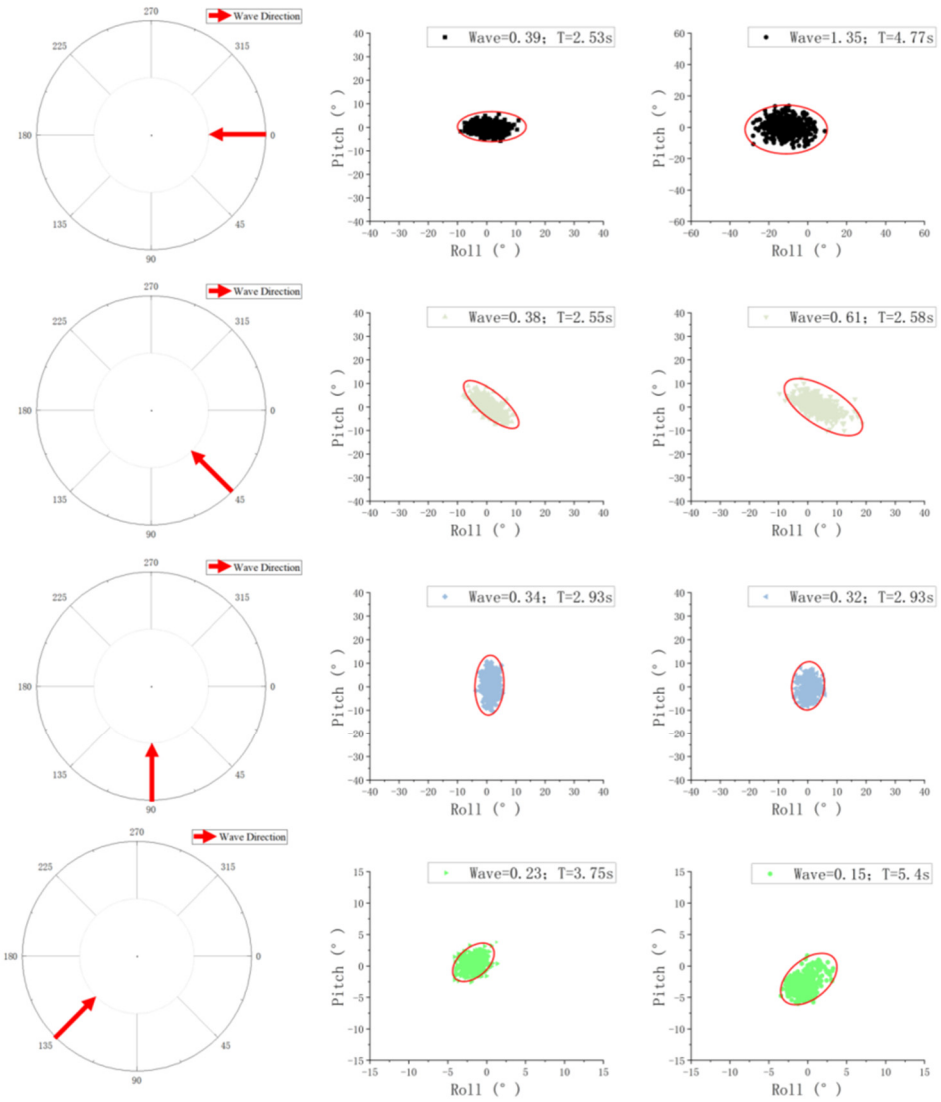

Figure 13. Distribution of buoy response with different incidence wave angle.

Following this, we conducted further analysis of the influence of wave height on buoy response. The area of the ellipse increases with the rise in wave height. Both pitch and roll responses of the buoy exhibit an upward trend with increasing wave height. Under severe wave conditions, the wet surface area of the buoy expands, and the alteration in the wet surface significantly affects the nonlinear hydrodynamic load, consequently leading to a substantial buoy response [38].

5. Conclusions

This paper proposes a new type of ocean observation system named the BCSOS, which enables continuous power and data transmission to the seafloor observation subsystem using solar energy and a buoy, eliminating the need for continuous onshore power transmission. The study conducted the following key activities.

First, the design and fabrication of the BCSOS were detailed, encompassing three main components: the RTEC Buoy, the PITS, and the SOS. The RTEC Buoy is equipped with a robust mechanical framework, engineered to endure harsh marine conditions. This framework is crucial for ensuring the buoy's stability and longevity. Additionally, the design of the buoy has been thoughtfully crafted to accommodate the placement of vital instruments such as solar panels, antennas, GPS devices, and internal lithium batteries. The structural design of the buoy adopts ANSYS for static structural checking to confirm its ability to withstand extreme ocean conditions. The PITS includes the design of cables and load-bearing structures. The cables are tested by experiments and simulation. The SOS is designed with the flexibility needed to carry a variety of instruments, which can be customized according to specific scientific needs and scenarios.

Secondly, the BCSOS was deployed at the Huangqi Peninsula. During maintenance, biological fouling has been observed across the entirety of the buoy base, with the joint of the buoy identified as the most susceptible area to failure during its operational lifecycle. Analysis of actual buoy response data, coupled with simulation results, has revealed that the stress concentrations at the joint can precipitate significant structural fatigue. The presence of numerous attached organisms exacerbates this issue. Consequently, it is imperative to enhance the anti-corrosion measures of the BCSOS, with particular emphasis on the joint areas. To fortify the buoy's stability, the design must be refined. Proposed enhancements include expanding the buoy's diameter and incorporating a counterweight to lower the center of gravity beneath the buoy. These adjustments are expected to increase the buoy's restoring moment and bolster its anti-overturning capacity.

Lastly, based on the recorded buoy data during the typhoon and regular operation, key parameters such as effective wave height, period, and buoy response were analyzed. There is a notable increase in wave height and period from the normal sea period to the typhoon period. The buoy's movement also increases drastically during the typhoon. Such heightened buoy response during the typhoon may result in repeated bending of the underlying cable connections, potentially leading to fatigue damage. Based on the classified wave height and buoy response data on the wave incident direction during operation, a significant regularity is observed in the distribution of the roll and pitch responses of the buoy, which appears elliptical with the change of the wave direction.

Overall, this paper presents a solution to deploying cabled seafloor observatories. However, it is important to note that the present design of our system is optimized for nearshore operations, where the deployment and maintenance are more feasible. While the system demonstrates potential for open ocean applications, further development and testing are required to ensure its suitability and reliability in more challenging offshore environments. catering to the requirements of scientific multidisciplinary observation

Author Contributions: Conceptualization, Y.L. (Yanjun Li) and W.Z.; methodology, W.Z., software, Y.Z. and W.Z.; validation, Y.L. (Yanjun Li) and Y.G.; formal analysis Y.Z. and W.Z.; investigation, D.C. and Q.J.; resources, D.C. and Q.J.; data curation, Q.J., D.C. and Y.Z.; writing—original draft preparation, W.Z.; writing—review and editing, Y.L. (Yanjun Li) and W.Z.; visualization, W.Z. and Y.Z.; supervision, Y.L. (Yanjun Li), Y.G. and Y.L. (Yuan Lin); project administration, Y.L. (Yanjun Li) and Y.G.; funding acquisition, Y.L. (Yanjun Li) and Y.G. All authors have read and agreed to the published version of the manuscript.

Funding: The work was jointly supported by the Hainan Provincial Joint Project of Sanya Yazhou Bay Science and Technology City (Grant No. 2021CXLH0020), the Natural Science Foundation of Hainan Province of China (Grant No. 623QN263), and the scientific and technological projects of Zhoushan (Grant No. 2022C01004).

Institutional Review Board Statement: Not applicable.

Informed Consent Statement: Not applicable.

Data Availability Statement: The original contributions presented in the study are included in the article, further inquiries can be directed to the corresponding authors.

Acknowledgments: The authors would like to express their gratitude to Jian Li from Hainan Institute, Zhejiang University, Xiaobo Zhang and Jian He from Hainan Provincial Observatory of Ecological Environment and Fishery Resource in Yazhou Bay for their invaluable technical support during the experiments.

Conflicts of Interest: The authors declare no conflicts of interest.

References

1. Qi, S.; Li, Y. A review of the development and current situation of marine environment observation technology and instruments. *Shandong Sci.* **2019**, *32*, 21–30. [CrossRef]
2. Lin, M.; Yang, C. Ocean Observation Technologies: A Review. *Chin. J. Mech. Eng.* **2020**, *33*, 1–18. [CrossRef]
3. Mao, K.; Gao, F.; Zhang, S.; Liu, C. An Information Spatial-Temporal Extension Algorithm for Shipborne Predictions Based on Deep Neural Networks with Remote Sensing Observations-Part I: Ocean Temperature. *Remote Sens.* **2022**, *14*, 1791. [CrossRef]
4. Wang, J.; Li, Y.; Yang, Y.; Liu, S.; Kong, Q.; Zheng, L. Status quo and trend of research and development in attitude measurement technology of ocean data buoy. *Oceanol. Limnol. Sin.* **2023**, *54*, 1239–1247. [CrossRef]
5. Fang, Z.; Chu, Y.; Feng, J. Application and prospect of unmanned surface vehicle in marine geological survey. *Mar. Geol. Lett.* **2020**, *36*, 72–77. [CrossRef]
6. Claustre, H.; Johnson, K.S.; Takeshita, Y. Observing the Global Ocean with Biogeochemical-Argo. *Annu. Rev. Mar. Sci.* **2020**, *12*, 23–48. [CrossRef] [PubMed]
7. Rudnick, D.L. Ocean Research Enabled by Underwater Gliders. *Annu. Rev. Mar. Sci.* **2016**, *8*, 519. [CrossRef] [PubMed]
8. Zhou, J.; Si, Y.; Chen, Y. A Review of Subsea AUV Technology. *J. Mar. Sci. Eng.* **2023**, *11*, 1119. [CrossRef]
9. Shu, C.; Lyu, F.; Xu, R.; Wang, X.; Wei, W. Technology Review of Cabled Ocean Observatories. *J. Mar. Sci. Eng.* **2023**, *11*, 2074. [CrossRef]
10. Zhai, F.; Li, P.; Gu, Y.; Li, X.; Chen, D.; Li, L.; Sun, L.; Liu, Z.; Jiang, Q.; Wu, W. Review of the research and application of the submarine cable online observation system. *Mar. Sci.* **2020**, *44*, 14–28.
11. Iannaccone, G.; Guardato, S.; Vassallo, M.; Elia, L.; Beranzoli, L. A New Multidisciplinary Marine Monitoring System for the Surveillance of Volcanic and Seismic Areas. *Seismol. Res. Lett.* **2009**, *80*, 203–213. [CrossRef]
12. Paul, W.; Bentley, D.; Chaffey, M.; Frye, D. Electrical and electro-optical mooring links for buoy based ocean observatories. In Proceedings of the 2003 International Conference Physics and Control. Proceedings (Cat. No.03EX708), Tokyo, Japan, 25–27 June 2003; pp. 201–206. [CrossRef]
13. Chen, J.; Zhang, D.; Wang, X.; Pan, X.; Wang, C.; Zhang, Z.; Ge, H. Research on the State-of-the-Art and Trends of Seafloor Observatory. *J. Ocean. Technol.* **2019**, *38*, 95–103.
14. S-NET. Available online: https://www.bosai.go.jp/inline/seibi/seibi01.html (accessed on 13 April 2024).
15. DONET. Available online: https://www.seafloor.bosai.go.jp/DONET/ (accessed on 8 May 2024).
16. Ocean Networks Canada. Available online: https://www.oceannetworks.ca/ (accessed on 8 May 2024).
17. Monterey Accelerated Research System (MARS) • MBARI. Available online: https://www.mbari.org/technology/monterey-accelerated-research-system-mars/ (accessed on 13 April 2024).
18. Ocean Observatories Initiative. Available online: https://oceanobservatories.org/ (accessed on 8 May 2024).
19. Home—The U.S. Integrated Ocean Observing System (IOOS). Available online: https://ioos.noaa.gov/ (accessed on 8 May 2024).
20. EMSO—Observing the Ocean to Save the Earth. Available online: https://emso.eu/ (accessed on 14 April 2024).
21. Introducing IMOS: IMOS.org.au. Available online: https://imos.org.au/ (accessed on 8 May 2024).
22. Zhang, S.; Tian, C.; Zhou, F. Design and optimization of buoy mooring with single-point cable for seafloor observatories. *Front. Mar. Sci.* **2023**, *9*, 1048048. [CrossRef]
23. Chen, Y. On the ocean observing methodology. *Acta Oceanol. Sin.* **2019**, *41*, 182–188. [CrossRef]
24. Zhang, S.W.; Tian, C.; Zhou, F.H. Ocean observation system design of mooring buoy and benthic node with electro-optical-mechanical cable. *Front. Mar. Sci.* **2022**, *9*, 1018751. [CrossRef]
25. SMART Cables. Available online: https://www.smartcables.org/ (accessed on 12 April 2024).
26. Chaffey, M.; Mellinger, E.; Paul, W. Communications and power to the seafloor: MBARI's Ocean Observing System mooring concept. In Proceedings of the MTS/IEEE Oceans 2001. An Ocean Odyssey. Conference Proceedings (IEEE Cat. No.01CH37295), Honolulu, HI, USA, 5–8 November 2001; pp. 2473–2481. [CrossRef]
27. Xi, F.; Pang, Y.; Liu, G.; Wang, S.; Li, W.; Zhang, C.; Wang, Z.L. Self-powered intelligent buoy system by water wave energy for sustainable and autonomous wireless sensing and data transmission. *Nano Energy* **2019**, *61*, 1–9. [CrossRef]
28. Gupta, S.; Gupta, S.; Singh, D.; Singh, D.; Yadav, A.; Yadav, A.; Jain, S.; Jain, S.; Pratap, B.; Pratap, B. A comparative study of 5083 aluminium alloy and 316L stainless steel for shipbuilding material. *Mater. Today Proc.* **2020**, *28*, 2358–2363. [CrossRef]
29. Ferraris, S.; Volpone, L.M. Aluminium alloys in third millennium shipbuilding: Materials, technologies, perspectives. In Proceedings of the Fifth International Forum on Aluminium Ships, Tokyo, Japan, 11–13 October 2005.
30. Orszaghova, J.; Wolgamot, H.; Draper, S.; Taylor, R.E.; Taylor, P.H.; Rafiee, A. Transverse motion instability of a submerged moored buoy. *Proc. R. Soc. A* **2019**, *475*, 20180459. [CrossRef]
31. Wang, J. *Principle and Ocean Data Buoys*; China Ocean Press: Beijing, China, 2013; ISBN 9787502787486.

32. CCS. *Classification Specification for Offshore Mobile Platform*; China Classification Society, 2023; Volume 56, p. 3. ISBN 1005-7560. Available online: https://www.ccs.org.cn/ccswz/specialDetail?id=202212260456159800 (accessed on 23 January 2024).
33. Amaechi, C.V.; Wang, F.; Ye, J. Investigation on hydrodynamic characteristics, wave-current interaction and sensitivity analysis of submarine hoses attached to a CALM buoy. *J. Mar. Sci. Eng.* **2022**, *10*, 120. [CrossRef]
34. Ghafari, H.; Dardel, M. Parametric study of catenary mooring system on the dynamic response of the semi-submersible platform. *Ocean Eng.* **2018**, *153*, 319–332. [CrossRef]
35. Faltinsen, O.M. *Sea Loads on Ships and Offshore Structures*; Shanghai Jiao Tong University Press: Shanghai, China, 2008; ISBN 9787313049384.
36. Yu, J.; Zhang, S.; Yang, W.; Xin, Y.; Gao, H. Design and Application of Buoy Single Point Mooring System with Electro-Optical-Mechanical (EOM) Cable. *J. Mar. Sci. Eng.* **2020**, *8*, 672. [CrossRef]
37. CFD Software: Fluid Dynamics Simulation Software. Available online: https://www.ansys.com/products/fluids (accessed on 8 May 2024).
38. ANSYS. *Aqwa Theory Manual*; Release 2023R1; ANSYS Inc.: Canonsburg, PA, USA, 2023.
39. Hasselmann, K.; Barnett, T.P.; Bouws, E.; Carlson, H.; Cartwright, D.E.; Enke, K.; Ewing, J.A.; Gienapp, H.; Hasselmann, D.E.; Kruseman, P.; et al. *Measurements of Wind-Wave Growth and Swell Decay during the Joint North Sea Wave Project (JONSWAP)*; Ergaenzungsheft Zur Deutschen Hydrographischen Zeitschrift, Reihe A; TU Delft: Delft, The Netherlands, 1973.
40. Shekar, V.; Caló, A.; Pongrácz, E. Experiences from seasonal Arctic solar photovoltaics (PV) generation-An empirical data analysis from a research infrastructure in Northern Finland. *Renew. Energ.* **2023**, *217*, 119162. [CrossRef]
41. Al-Wreikat, Y.; Serrano, C.; Sodré, J.R. Effects of ambient temperature and trip characteristics on the energy consumption of an electric vehicle. *Energy* **2022**, *238*, 122028. [CrossRef]
42. Amaechi, C.V.; Chesterton, C.; Butler, H.O.; Wang, F.; Ye, J. An Overview on Bonded Marine Hoses for sustainable fluid transfer and (un) loading operations via Floating Offshore Structures (FOS). *J. Mar. Sci. Eng.* **2021**, *9*, 1236. [CrossRef]
43. Liang, X. Eastern China on Alert as Typhoon Doksuri Makes Landfall in Fujian. South China Morning Post 2023. Available online: https://www.scmp.com/news/china/science/article/3229295/eastern-china-alert-typhoon-doksuri-makes-landfall-fujian (accessed on 23 January 2024).